High-current fast electron beam propagation in a dielectric target

Ondrej Klimo*
Faculty of Nuclear Sciences and Physical Engineering, Czech Technical University in Prague, Brehova 7, 115 19 Praha 1, Czech Republic

V. T. Tikhonchuk and A. Debayle
Centre Lasers Intenses et Applications, UMR 5107, CNRS-CEA-Université Bordeaux 1, 33405 Talence Cedex, France
(Received 26 June 2006; published 17 January 2007)

Recent experiments demonstrate an efficient transformation of high intensity laser pulse into a relativistic electron beam with a very high current density exceeding 10^{12} A cm^{-2}. The propagation of such a beam inside the target is possible if its current is neutralized. This phenomenon is not well understood, especially in dielectric targets. In this paper, we study the propagation of high current density electron beam in a plastic target using a particle-in-cell simulation code. The code includes both ionization of the plastic and collisions of newborn electrons. The numerical results are compared with a relatively simple analytical model and a reasonable agreement is found. The temporal evolution of the beam velocity distribution, the spatial density profile, and the propagation velocity of the ionization front are analyzed and their dependencies on the beam density and energy are discussed. The beam energy losses are mainly due to the target ionization induced by the self-generated electric field and the return current. For the highest beam density, a two-stream instability is observed to develop in the plasma behind the ionization front and it contributes to the beam energy losses.

DOI: 10.1103/PhysRevE.75.016403 PACS number(s): 52.40.Mj, 52.57.Kk, 52.65.Rr

I. INTRODUCTION

In recent years, generation of high current relativistic electron beams in short-pulse high intensity laser interactions with solid targets and the propagation of these beams in dense matter have been studied both theoretically [1,2] and experimentally [3–5]. One of the important applications of laser-produced relativistic electron beams is the fast ignition approach to the inertial confinement fusion [6]. A number of physical processes may dissipate energy of the electron beam or inhibit its collimated propagation into the dense target core. This would limit the quality or position of the energy deposition. The processes associated with the return current are among the most important ones. These are the filamentation, the Weibel, and the two-stream instabilities [7,8]. Recently, the ionization instability associated with high current electron beam propagation in nonconducting materials has been identified [9,10].

The ionization is an important process in the propagation of relativistic electron beam in dielectric material as it provides free charges for the beam charge and current neutralization. Three ionization processes may contribute to increase the number of free electrons. Namely, the collisional ionization by the beam electrons, the ionization by the self-consistent electric field, and the collisional ionization by the return current electrons. The energy of newborn electrons is as low as several eV initially and therefore they form a separate population distinct from the beam electrons. These cold electrons form the return current which is highly collisional.

Theoretical models describing the ionization processes induced by high current electron beam in dielectric targets have been discussed recently in [9,11]. In particular, the effect of the field ionization in the head of the electron beam was identified as a dominant process which defines the effective velocity of the beam propagation and its energy losses.

The complexity of the beam electron distribution function, the nonlinearity of ionization processes, and the transition of the initially cold neutral material into a dense warm plasma make it difficult to describe the whole process of beam propagation using only analytical models. The numerical simulations provide important information here. Moreover, when the laser pulse duration is of the order of tens of femtoseconds, the beam length is so short that the asymptotic approach frequently used in the theoretical analysis might not be completely appropriate.

However, complete kinetic simulations of the beam propagation are not yet accessible because of a large disparity between the densities and the electron energies of the beam and the solid material. The recently developed hybrid models [12–14] treat cold electrons in a fluid approximation and ignore the electrostatic fields, which develop on the Debye scale length. This might be appropriate for metals but is not sufficient for dielectrics. Here we present a fully kinetic simulation model based on the particle-in-cell (PIC) algorithm adapted for studies of the fast electron beam propagation in a solid density plastic material. This model is described in detail in Sec. II. To keep the computational cost of the simulations on a reasonable level, some simplifying assumptions are made. Their validity is discussed there. In Sec. III, we present a quasistationary analytical model which describes the electric field structure and the ionization processes induced by the beam. It applies the results obtained in previous publications [9,11] to the specific fast electron distribution function used in simulations and accounts also for the plasma electron heating, the collisional ionization, and the electron beam instability. The results of the simulations and their comparison with the analytical model are discussed

*Electronic address: klimo@watt.fjfi.cvut.cz

in Sec. IV. Finally, in Sec. V, we summarize the main results of this paper and present our concluding remarks.

II. NUMERICAL MODEL

To simulate electron beam propagation in dielectric targets, we use a relativistic electrostatic PIC code in one spatial dimension and in three dimensions in the phase space. It evolved from the electromagnetic code LPIC++ [15]. The original code was modified to account for additional physical effects. The beam and plasma electrons are treated as separate species. Since the collisions of fast electrons are neglected, we keep only one velocity component of the beam particles and we take into account only the electric field component in the direction of the beam propagation. The neutral atoms and ions are treated as an immobile stationary background. This crucial simplification is justified by two arguments: First, the amplitude of the self-consistent electric field remains always well below the atomic field; second, its existence in any particular place is temporally limited to the duration of the ionization front, which is not more than ten fs. Therefore, the atoms and ions intervene only in the ionization and the collisional parts of the code.

The simulation box consists of two spatial regions of different solid density materials. The first one is the injection region—a thin aluminum foil, where the electron beam is initiated. It is followed by the propagation region composed of plastic (polyethylene). The length of the injection layer is equal to the beam length, which is 8 μm in the examples presented below, and it contains both cold and beam electrons. The number density of cold electrons is 1.8×10^{23} cm^{-3}, corresponding to the solid density aluminum with three free electrons per ion. The initial electron temperature of cold aluminum electrons is set to 50 eV. The beam electrons are distributed among the cold ones and they are assigned a velocity, uniformly distributed between 0.7 and 0.9 speed of light, in the beam propagation direction. The density of electrons in the beam is also initially uniform along the propagation direction except for the first and the last micron where it linearly increases or decreases, respectively. As the density of the beam in this study, 10^{18}–10^{20} cm^{-3}, is much lower than that of solid aluminum and as the number of beam electrons is desired to be high enough to have a good statistics of their distribution function and a smooth profile of the electric field, we initiate these electrons with a lower numerical weight and keep the number of macroparticles comparable for cold and hot electrons.

The size of the computational cell as well as the time step used in the simulation should be proportional to the electron Debye length which depends on the electron density and temperature. The Debye length in a real low temperature solid density aluminum plasma is about 0.1 nm which is beyond our available computational resources. However, what happens in the aluminum layer is not important in our study except for a short time at the beginning until the beam leaves it. Moreover, the plasma, which develops during the beam propagation in plastic, is of lower density. For these reasons, we consider a higher initial electron temperature in Al, about 50 eV, and we are using the cell size of 1 nm. In the future, it would be possible to implement a more sophisticated weighting algorithm for field interpolation and current density assignment to the cells into our code. This would allow us to avoid a numerical heating. Nevertheless, the present calculations provide a sufficient accuracy. The total energy in the simulation box does not deviate from the initial value more than 1% during the whole simulation. The plastic layer is usually 50 μm long and it contains only neutral atoms initially. The two most important processes which take place in this part of the simulation box during the electron beam propagation, the ionization, and the collisions of newly produced cold electrons, are described next.

A. Ionization

According to our initial conditions and to estimates on the importance of individual ionization processes during the fast electron beam propagation in dielectrics [11], ionization by the electric field significantly dominates collisional ionization by the beam electrons at the head of the beam. The collisional ionization by the beam electrons is therefore neglected in our model. On the other hand, the collisional ionization by the return current electrons is indeed very important. The field ionization at the head of the beam creates a seed population of free electrons which gain their energy from the electric field. The kinetic energy of the newborn free electrons rapidly overcomes the threshold for collisional ionization and the population of free electrons increases further several times. If the collisional ionization by the return current electrons is not taken into account, the resistivity of plasma generated in the plastic target is too high and the beam energy is dissipated by the Ohmic heating rapidly. As we are dealing with simulation times of the order of tens of femtoseconds and the neutral target is usually not completely ionized during this time, the complementary process of three body recombination has been omitted.

1. Electric field ionization

The field ionization process is included in the PIC code using a Monte Carlo algorithm [16]. To calculate the ionization rate, we use the formula derived by Ammosov, Delone, and Krainov (ADK) [17]

$$w_{\mathrm{fi}}(E) = \nu_a \left(\frac{E_a}{E}\right)^b \exp\left(-a\frac{E_a}{E}\right), \tag{1}$$

where E is the local electric field and the other parameters characterizing the target material are

$$\nu_a = 1.61\omega_{\mathrm{a.u.}} Z^2/n_{\mathrm{eff}}^{4.5}, \quad E_a = 10.87 E_{\mathrm{a.u.}} Z^3/n_{\mathrm{eff}}^4,$$

$$b = 2n_{\mathrm{eff}} - 1.5, \quad a = 0.0613 n_{\mathrm{eff}}.$$

Here $E_{\mathrm{a.u.}} = e/4\pi\epsilon_0 a_B^2 = 514$ kV/μm is the atomic electric field, $\omega_{\mathrm{a.u.}} = eE_{\mathrm{a.u.}} a_B/\hbar = 41$ fs^{-1} is the atomic frequency, $a_B = 4\pi\epsilon_0\hbar^2/m_e e^2$ is the Bohr radius, Z is the ion charge seen by the electron being released, $n_{\mathrm{eff}} = Z\sqrt{U_H/U_i}$ is the main effective quantum number, U_i is the ionization potential of the corresponding ion, and $U_H = (1/2)eE_{\mathrm{a.u.}} a_B = 13.6$ eV is the ionization potential of hydrogen.

We assume that only the outermost shell of carbon atoms can be ionized ($Z=1$) and for the ionization potential we use an average value between carbon and hydrogen, $U_i = 12.8$ eV. This approximation seems to be quite reasonable because the dependence of the ionization probability on the ionization potential is highly nonlinear and secondary ionization does not set up. The simulation results do not depend on the ionization potential if we vary it in the domain between the values for carbon and hydrogen. The field in our simulations is always lower than the critical field at which the barrier suppression ionization sets up [18]. Therefore, application of the ADK tunneling ionization rate is valid.

The difference in the numerical weight of the beam and cold electrons must not be too big, otherwise a single cold electron would affect the electric field too much. On the other hand, the number of new free electrons per simulation cell is limited by the computational performance. As we will show later, the final ionization state of the initially neutral plastic target depends on the beam density. Roughly, the density of the plasma created by the beam is 1000 times higher than the beam density. Consequently, we are using 4000, 1000, and 400 cold electrons per simulation cell to represent a singly ionized solid density plastic (polyethylene) for the beam densities 10^{18}, 10^{19}, and 10^{20} cm^{-3}. Then the number of cold electrons per simulation cell in plasma behind the beam is usually in the reasonable range of values between 70 and 400.

We recall here that in our simulations atoms and ions are treated as immobile and they serve only to provide an appropriate resolution for sampling the ionization probability. Using the same number of atoms per cell as the number of cold electrons would impose unnecessary constrains on the computational performance. For this reason, we use just 200 equally spaced atoms per cell in every simulation and let each of these atoms be ionized several times, strictly speaking 20, 5, and 2 times, with the same ionization potential. The atoms "remember" how many times they were already ionized and when the ionization probability for the electric field ionization is calculated, it is always multiplied by the number of electrons that can still be released from the corresponding atom. If the ionization takes place, a new electron is injected into the simulation box at the corresponding place and it is initiated with velocity sampled from the Maxwellian distribution with temperature 7 eV. The nonzero initial velocity does not affect much the overall energy balance but it is essential for the collisional algorithms.

The energy spent for ionization is subtracted from the field using an artificial ionization current. This current is directed along the electric field and its amplitude is given by $j_{\mathrm{ion}}=W_{\mathrm{ion}}/E$, where W_{ion} is the energy spent on ionization per unit volume and unit time step. Before the ionization takes place we always ensure that the field still has enough energy to ionize another atom and, if not, the ionization process is suppressed. In our simulations, the part of the field energy spent into ionization is indeed important. In the runs where the ionization current was neglected, the field amplitude and correspondingly the number of new free electrons at the head of the beam were significantly higher.

2. Collisional ionization

The collisional ionization is implemented in the code using a Monte Carlo approach too. The probability that an electron ionizes an atom during the time step of Δt is calculated as $P_{\mathrm{ci}}=1-e^{-\nu_{\mathrm{ci}}\Delta t}$, with ν_{ci} being the frequency of collisional ionization. This frequency is calculated for every electron as

$$\nu_{\mathrm{ci}} = v_e n_a \sigma_{\mathrm{ci}}, \tag{2}$$

where v_e is the electron velocity, n_a is the number density of atoms that can be ionized, and σ_{ci} is the cross section for electron impact ionization. This cross section is calculated using an analytical fit to the Bethe binary encounter cross section [19] for the ionization of polyethylene. Currently, we assume that only the outermost shell of carbon atoms can be ionized. This assumption is valid for the beam densities below 10^{20} cm^{-3}. For higher densities it is not exactly correct, as at the rear part of the beam the single ionization is almost completed, while the temperature of cold electrons is sufficiently high for the secondary ionization of carbon atoms. This assumption could be easily corrected in the future; however, we are not considering such very high beam densities here.

When the collisional ionization takes place, we choose randomly an atom which will be ionized in the same cell and release an electron. It is injected into the simulation box in the same place as the atom with the energy randomly sampled from the Maxwellian distribution with temperature 2 eV. The ionization energy and the kinetic energy of the released electron are both subtracted from the kinetic energy of the electron that ionized the atom. The collisional ionization leads to plasma cooling as a counterpart of the joule heating by the return current.

B. Collisions

As most of the collisional algorithms for PIC codes are computationally very expensive, we are not using collisions for every species of particles. All ions and atoms are immobile and therefore collisionless. Moreover, we assume their temperature to be low during the beam propagation and therefore they are having zero velocities. The beam electrons are also considered as collisionless, as it was explained in the beginning of this section. The cold electrons in aluminum are highly collisional but the aluminum layer is included just to provide initial conditions for the fast electrons and to avoid the beam disruption at the boundary between the two materials. Therefore, there is no need to know their distribution function exactly. They have initially a Maxwellian distribution and the joule heating in aluminum is insufficient to heat them up or to change their distribution significantly. However, their collisions must be taken into account to damp the oscillations at plasma frequency that are otherwise present. We treat their collisions with ions with a constant collisional frequency of 2 fs^{-1}. This value is realistic and it is sufficient to damp the oscillations, but does not inhibit the return current in aluminium. Therefore the cold electrons in plastic is the only species for which collisions are essential and must be treated carefully.

1. Elastic electron-atom scattering

Collisions are included into the code using a Monte Carlo approach [20]. This algorithm is suitable for both types of

collisions—the collisions of electrons with neutral atoms and the Coulomb collisions with ions and other cold electrons. Collisions with neutral atoms play the most important role at the front of the electron beam, where electron and ion densities and also the Coulomb collision frequency are low. If collisions with neutral atoms are not included, cold electrons would gain too high velocity from the field just after ionization and the electric field behind the ionization front starts to oscillate at the plasma frequency. Because of higher velocities, electrons are less collisional during the whole simulation in this case and plasma oscillations are damped only slowly. The frequency of collisions with neutral atoms is calculated using the total cross section for elastic electron scattering in plastic (polyethylene) as $\nu_{\mathrm{en}}=v_e n_m(\sigma_{\mathrm{C}}+2\sigma_{\mathrm{H}})$, where n_m is the number density of CH_2 molecules, which is initially 0.3×10^{23} cm^{-3}, and σ_{C} and σ_{H} are the total cross sections for elastic scattering with carbon and hydrogen, respectively. For electron energies above 100 eV, we use the values for σ_{C} and σ_{H} from [21] which are calculated using the Dirac partial wave method with screened potentials obtained from Dirac-Hartree-Fock atomic electron densities. As there are no precise data for the energy range below 100 eV, we suppose that the collisional frequency is constant there. The value of this frequency is 5 fs^{-1} for the neutral plastic. This assumption is not too restrictive since it takes 0.16 fs for a 10 eV electron to fly from one atom to another. Therefore the maximum collisional frequency cannot be more than 6 fs^{-1}. The collisional frequency slowly decreases for energies above 100 eV. For example, the frequency is 4 fs^{-1} for a 300 eV electron. The correctness of our Monte Carlo approach for such high collisional frequencies is guaranteed by a very short simulation time step of the order of 10^{-3} fs.

The angular shape of the effective cross section of electron-atom collisions used here depends on the electron energy and has the following form:

$$\frac{d\sigma_{\mathrm{en}}}{d\cos\chi}=\frac{\sigma_T\varepsilon}{4\pi[1+\varepsilon\sin^2(\chi/2)]\ln(1+\varepsilon)}, \tag{3}$$

where χ is the deflection angle, ε is the electron kinetic energy in eV, and σ_T is the corresponding integral cross section for the carbon and hydrogen. This analytical expression was used to describe the screened Coulomb collisions in [22] and it captures the main features of electron-neutral scattering: It is approximately isotropic at low energies and it becomes increasingly anisotropic as the energy increases.

The probability of elastic collision with an atom was sampled for each electron at each time step. The details about random sampling of the deflection angle and calculation of postcollision velocities of electrons are given in the Appendix.

2. Coulomb collisions

The Coulomb electron-ion and electron-electron collisions set up behind the ionization front where the density of free electrons and ions is high enough. They are treated here as binary collisions using the same collisional algorithm [20]. Electrons collide in pairs; in electron-ion collisions we use again the assumption of static scattering centers. Therefore, there is no need to group ions in pairs with electrons. The validity of this algorithm for simulation of Coulomb collisions in plasma was proved by its first order correspondence to solving the Landau-Fokker-Planck collisional integral [23]. In comparison with electron-neutral collisions, the main difference is that these collisions take place for every electron every time step and the deflection angle between precollision and postcollision velocities depends on the collisional frequency.

The angular dependence of scattering due to the Coulomb collisions into an angle χ is given as

$$\frac{d\sigma_e}{d\cos\chi}=\frac{A\sigma_e}{2\pi}e^{-A(1-\cos\chi)}, \tag{4}$$

where the factor $A\simeq 1/\nu_e\Delta t\gg 1$ accounts for the finite time step. The value of Spitzer collisional frequency ν_e depends on the local cold electron density and electron velocity. In practical units $\nu_e=1.6\times10^6 n_e v_e^{-3}$ s^{-1}, where the electron velocity is in m/s and the electron density is in m^{-3}. In our code the electron collisional frequency was kept in the range 1–1000 ps^{-1}.

The procedures of random sampling of the distribution for the deflection angle and calculation of postcollision velocities are described in the Appendix.

III. ANALYTICAL MODEL OF THE BEAM PROPAGATION

The propagation of the ionization front induced by the electron beam is described within a simplified one-dimensional model. It is inspired by the previous publication [9]. However, the distribution function for fast electrons is different. A more detailed kinetic analysis of the beam in the ionization front enables us to highlight several physical mechanisms important in the beam propagation. The energy losses of the beam electrons due to the self-consistent electric field in the ionization front and in the beam tail are analyzed as well as the plasma heating. Moreover, as the density of the beam in our paper is higher than in [9], the ionization by the self-consistent electric field is the dominant ionization mechanism in the beam front.

The propagation model can be described as follows. The electron beam penetrates the neutral plastic target and creates an electric field along its propagation direction. This electric field slows down the beam electrons, while reaching values sufficiently high to ionize the matter. The thermal electrons spawning from ionization propagate backward and neutralize the charge and the current of the electron beam behind the ionization front. The total current becomes sufficiently low to allow the rest of the beam to propagate through.

The analytical model assumes a quasistationary propagation where all parameters vary slowly in the reference frame of the ionization front. It divides the electron beam into two parts. The beam head (or the ionization front) where the matter is supposed to be ionized by the electric field, and the beam body behind the ionization front where the current neutralization has been set up. In the first part of this section we will describe the beam front characteristics and particularly the front velocity which depends on the beam density and the

current. The collisional ionization, which takes place in the beam tail, will be considered after that.

It is important to make a distinction between the maximum electron velocity, $v_{\max}$, and the velocity of the ionization front v_f which can be regarded as a mean propagation velocity of the beam. Following [9], the structure of the ionization front can be better described in the front reference frame. Similarly to simulations the injected beam distribution function is a constant in the interval $\Delta v = v_{\max} - v_{\min}$ between the minimum $v_{\min}$ and the maximum $v_{\max}$ velocities. In the momentum space, $p_x = \gamma m_e v_x$, with the electron relativistic factor, $\gamma = (1 - v_x^2/c^2)^{-1/2}$, the distribution function of the beam can be written as

$$f_b(p_x) = \frac{n_{b0}}{\Delta v} H(p_{\max} - p_x) H(p_x - p_{\min}) \frac{dv_x}{dp_x}, \tag{5}$$

where H is the Heaviside step function. Assuming that the beam electrons are nonrelativistic in the front reference frame, one has $dv_x/dp_x \simeq 1/m_e \gamma_f^3$, where $\gamma_f = (1 - v_f^2/c^2)^{-1/2}$.

A. Velocity of the ionization front

The fast electrons are described by the stationary Vlasov equation

$$v_x' \frac{\partial f_b'}{\partial x'} - eE \frac{\partial f_b'}{\partial p_x'} = 0, \tag{6}$$

which gives the beam distribution function $f_b'(m_e \gamma' c^2 - e\varphi)$ with the electric field $E = -d\varphi/dx'$ and $\gamma' = \sqrt{p'^2/m_e^2 c^4 + 1}$. The prime indicates the front reference frame. The electric field is described by the Poisson equation

$$\epsilon_0 \frac{dE}{dx'} = e(n_i' - n_e' - n_b'), \tag{7}$$

where n_b', n_e', and n_i' are the densities of the beam electrons, the cold electrons, and the ions, respectively. They are defined by the continuity equations

$$-v_f \frac{dn_i'}{dx'} = \frac{d\left[n_e'(u_e' - v_f)\right]}{dx'} = w_{\text{fi}} n_a, \tag{8}$$

where we suppose a weak ionization, $n_a \gg n_i$. The electric field ionization rate w_{fi} is described by the ADK formula (1). The cold electron velocity u_e' is defined by the mobility equation and the electron collision frequency ν_e is supposed to be constant in the analytical model. In the front reference frame this equation reads

$$u_e' = -eE/m_e \gamma_f^2 \nu_e. \tag{9}$$

From Eqs. (8) and (9) one finds the charge separation $\delta n' = n_i' - n_e' = n_i' u_e'/v_f$.

The electric field is always positive, therefore the potential decreases monotonously from the beam source ($\varphi = 0$) to its head ($\varphi = \varphi_{\min}$). Then the governing equations can be further simplified by considering the dimensionless electric field potential $\phi = e\varphi/m_e c^2$ as an independent variable [9]

$$\epsilon_0 E \frac{dE}{d\phi} = m_e c^2 \left(n_b'(\phi) - \frac{eE}{m_e \gamma_f^2 \nu_e v_f} n_i' \right), \tag{10}$$

$$\frac{dn_i'}{d\phi} = \frac{m_e c^2 n_a w_{\text{fi}}}{e v_f E}. \tag{11}$$

Only electrons moving with velocity higher than v_f can penetrate the front. Therefore, only these electrons contribute to the field formation. These electrons slow down in the front, turn around, and finally come back. The fastest ones reach the minimum potential $\phi_{\min} = -(\gamma_{\max}' - 1)$. The electron relativistic factor in the front frame is given by the Lorentz transformation $\gamma_{\max}' = \gamma_f(\gamma_{\max} - \beta_f \sqrt{\gamma_{\max}^2 - 1})$. Thus the distribution function in the beam head is even in the front reference frame. The formula for the beam density, $n_b'(\phi) = \int f(\gamma' - \phi) d p'$, reads

$$n_b'(\phi) \approx \frac{2 n_{b0} c}{\Delta v \gamma_f^3} \sqrt{2(\phi - \phi_{\min})}. \tag{12}$$

The field ionization rate (1) is a very sharp function of the electric field. Therefore, the plasma density increases very quickly and the right-hand side of the Poisson equation changes its sign when the electric field reaches its maximum. The maximum value of the electric field, E_m, at the point ϕ_m follows from the Poisson equation (10)

$$eE_m = m_e \nu_e v_f \gamma_f^2 n_b'(\phi_m)/n_i'(\phi_m). \tag{13}$$

Near this maximum the electric field can be approximated as a quadratic function [9]

$$E(\phi) = E_m - \frac{\alpha_E}{2}(\phi - \phi_m)^2, \tag{14}$$

where

$$\alpha_E \approx \frac{m_e c^2 n_a}{\epsilon_0 E_m \nu_e \beta_f^2 \gamma_f^2} w_{\text{fi}}(E_m). \tag{15}$$

Here the derivative of the beam density is neglected because at this point it is weakly perturbed. This approximation for the electric field allows one to integrate Eqs. (10) and (11) between $\phi_{\min}$ and ϕ_m and obtain the expressions for E_m and $n_i(\phi_m)$

$$\epsilon_0 E_m^2 = \frac{8\sqrt{2}}{3} \frac{n_{b0} m_e c^3}{\gamma_f^3 \Delta v} (\gamma_{\max}' - 1)^{3/2},$$

$$n_i'(\phi_m) = \frac{\epsilon_0 \nu_e \beta_f \gamma_f^2 E_m}{ec} \sqrt{\frac{\pi \alpha_E}{2 a E_a}}. \tag{16}$$

In the integration of the Poisson equation the contribution of the plasma density was neglected.

One has to know the beam density $n_b'(\phi_m)$ in order to resolve these equations and to find the front velocity. Assuming that the beam losses behind the front are relatively small one can make an approximation $n_b'(\phi_m) \approx n_b'(0)$. Then from Eqs. (13), (16), and (17), the front velocity v_f is defined as

$$n_{b0} = \left[\frac{a E_a}{(1+b)G} W\left(-1, \frac{a E_a}{(1+b) L^4 G^4} \right)^{1/(1+b)} \right]^2, \tag{17}$$

where

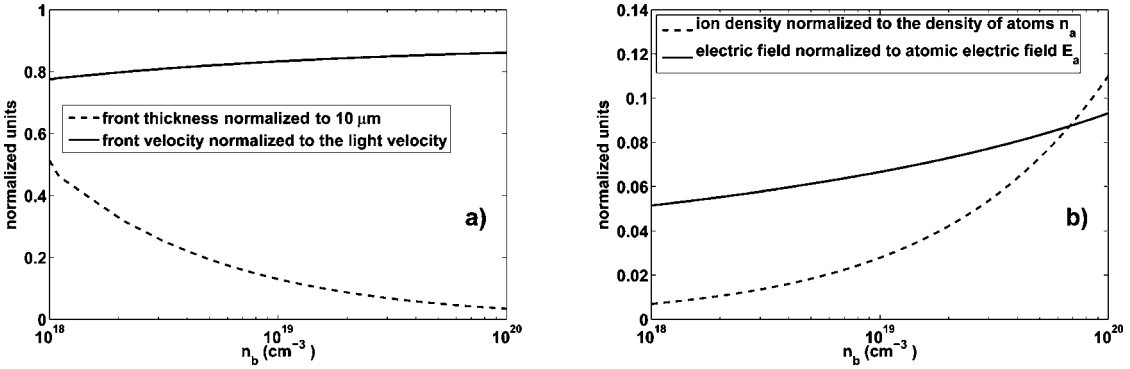

FIG. 1. Dependence of the front velocity [(a) solid line], the front thickness [(a) dashed line], the maximum ion density [(b) dashed line], and the maximum electric field [(b) solid line] on the beam density. The parameters are $v_{\min}=0.7c$, $v_{\max}=0.9c$, and $\nu_e=5$ fs^{-1}. The density of the electron beam is varied from $n_{b0}=10^{18}$ to 10^{20} cm^{-3}.

$$G(v_f)=\sqrt{\frac{8\sqrt{2}m_e c^3}{3\epsilon_0\gamma_f^3\Delta v}}(\gamma'_{\max}-1)^{3/4}, \tag{18}$$

$$L(v_f)=\frac{16am_e\nu_e c^2 v_f^2(\gamma'_{\max}-1)}{\pi\epsilon_0\nu_a n_a E_a^{b-1}\gamma_f^5\Delta v^2} \tag{19}$$

and $W(-1,x)$ is the Lambert W function defined on the interval $[-e^{-1},0]$ as an inverse of xe^x. Knowing the front velocity, one can find the maximum of the electric field E_m from Eq. (16) and the maximum plasma density after ionization $n'_{i\,\max}\approx 2n'_i(\phi_m)$ from Eq. (17). The field ionization takes place in the vicinity of ϕ_m, where the electric field achieves its maximum.

One can also define the thickness of the front Δx_f as a distance between the head of the beam and the maximum of the electric field. Here the electric charge is accumulated in order to ionize the matter. Integrating Eq. (10) over $[\phi_{\min},\phi]$ one finds $E(\phi)=E_m(1-\phi/\phi_{\min})^{3/4}$ which gives the potential distribution in the front

$$\phi/\phi_{\min}=1-(1-x'/\Delta x'_f)^4. \tag{20}$$

Then the following formula for the front thickness $\Delta x_f=\Delta x'_f/\gamma_f$ can be derived:

$$\Delta x_f=\frac{4m_e c^2}{eE_m\gamma_f}(\gamma'_{\max}-1). \tag{21}$$

For the parameters of our simulations, it is of the order of a few μm.

In the front reference frame the electric field structure is stationary and therefore its energy does not change in time. However, the dissipated energy is nonzero in the laboratory frame for two reasons. First, the current in the ionization front is nonzero, $j_{\rm bf}=en'_b v_f\gamma_f$, and therefore there is the joule dissipation across the front, $j_{\rm bf}\varphi'_{\max}/\gamma_f$. Second, one should take into account the energy spent for the ionization [11], which is $n_{i\,\max}U_i$. Here $n_{i\,\max}=2n'_i(\phi_m)/\gamma_f$ is the ion density behind the ionization front. Then the energy dissipation rate in the ionization front $W_{\rm bf}$ can be expressed as

$$W_{\rm bf}=n_{i\,\max}U_i v_f+n'_b v_f e|\varphi'_{\min}|. \tag{22}$$

Although this is a relatively small part of the beam energy flux, $q_b\simeq n_b v_{\max}m_e c^2(\gamma_{\max}-1)$, one should be aware that these are the electrons in the front that are suffering this dissipation and after losing a substantial part of their energy, they are falling back and are substituted by fresh electrons from the tail. This energy redistribution is clearly seen in the simulations.

The dependencies of the ionization front characteristics on the electron beam density for the parameters used in the simulations are shown in Fig. 1. The front velocity increases with the beam density. For the beam densities below 10^{18} cm^{-3}, it becomes smaller than the minimum beam velocity and our quasistationary model is no longer valid. The front thickness is a decreasing function of n_{b0}. The maximum electric field very weakly depends on the beam density. It is of the order of 5% of the atomic field $E_{\rm a.u.}$. The maximum ion density $2n_i(\phi_m)$ is about 100 times higher than the beam density but still even at high beam densities the ionization in the front is always incomplete [11]. This comes from the fact that even a small number of newborn electrons quickly screens the electric field and the ionization process is suppressed.

Knowing the profile of the potential (20), one can check the validity of our hypothesis about the stationary ionization front. The relaxation time to reach this quasistationary state is the time for an electron to cross the ionization front, $\Delta t_r\simeq\int dx/v_b(x)$. It follows from the electron equation of motion that $t_r=2\gamma_f^{3/2}(m_e\Delta x_f/e\langle E\rangle)^{1/2}$, where $\langle E\rangle$ is the mean electric field seen by the electron. For the fastest electrons, this time is very long and some of them can escape the front. However, slower electrons are falling back much quicker as they see a higher mean electric field, close to E_m. One can show that for more than 60% of electrons, the return time is shorter than 35 fs. That justifies our quasistationary approach for realistic beam parameters.

B. Collisional processes behind the ionization front

Another important limitation of our model of the ionization front is the hypothesis that $|\phi_m|\ll|\phi_{\min}|$. Therefore, one

should verify that the potential drop in the beam body is sufficiently small. According to the Poisson equation (10), the electric field behind the front drops down to about half its maximum E_m and then the field ionization stops and the ion density saturates at the level $n'_{im}(0) \approx 2n'_{im}$. Such a field will provide a very large potential drop as the beam length is much larger than the front thickness. However, the ionization process does not stop behind the ionization front. The joule dissipation behind the front leads to electron heating and then the collisional ionization takes place.

The electric field, the electron temperature, and the ionization level can be found using a quasistationary model based on two assumptions: (i) The current neutralization, $j_b + j_e \simeq 0$, is established immediately after the ionization front and (ii) the joule heating is equilibrated by the collisional ionization

$$C_e \frac{\partial T_e}{\partial t} = j_e E - \alpha_i U_i \frac{\partial n_i}{\partial t} \simeq 0, \tag{23}$$

where C_e is the electron heat capacity, the coefficient $\alpha_i \sim 2$–5 accounts for additional energy losses in inelastic collisions [25], and $j_e = -e^2 n_e E / m\nu_e$ is the return current following from the equation of electron mobility (9). The electron density is defined by the quasineutrality condition, $n_e \simeq n_i$, and the collisional ionization [24]

$$\frac{\partial n_e}{\partial t} = \nu_{\rm ci} n_e, \quad \text{where } \nu_{\rm ci} \simeq n_a \sigma_{\rm ci} \sqrt{U_i/m_e} \exp(-U_i/T_e). \tag{24}$$

The collision ionization cross section $\sigma_{\rm ci}$ was discussed in Sec. II A 2, Eq. (2). This formula is valid for $T_e < U_i$ where the ionization probability is an exponential function of the electron temperature. The three-body recombination, according to Ref. [24], depends on the electron density and temperature as $n_e^2 T_e^{-9/2}$. It can be neglected for electron temperatures above 1 eV and on the time scale smaller than a few ps, in which we are interested here.

An approximate solution to Eqs. (23) and (24) is rather straightforward. Supposing that the overall potential drop in the beam tail is small, $|\phi_m| \ll |\phi_{\rm min}|$, the beam current is constant. Then Eq. (23) provides a relation between the electron temperature and the density: $\nu_{\rm ci}(T_e) \simeq m_e \nu_e j_b^2 / e^2 n_e^2 \alpha U_i$, while Eq. (24) provides the spatial distribution of the plasma density. Supposing that the density right behind the ionization front ($x = x_f$) is known, one obtains

$$n_i(x) \simeq \sqrt{n_{i\,\max}^2 + \frac{j_b^2 m_e \nu_e}{e^2 \alpha U_i v_f}(x_f - x)}. \tag{25}$$

The second term in this equation, which accounts for the collisional ionization, typically dominates. This means that the plasma density increases as the square root of the distance from the front and consequently the electric field decreases as the square root of that distance. In particular, in the case of a high current electron beam, the electric field in the beam tail can be estimated as $eE \simeq \sqrt{m_e \nu_e \alpha U_i v_f / (x_f - x)}$ and consequently the potential drop is $e\varphi_m \simeq -2\sqrt{m_e \nu_e \alpha U_i v_f x_f}$. This estimate allows us also to write down the condition of applicability of our model,

$$2\sqrt{m_e \nu_e \alpha U_i v_f x_f} \ll m_e c^2 (\gamma_{\max} - 1), \tag{26}$$

which is also the condition of efficient electron beam transport across the dielectric target. Otherwise, this condition could be considered as an estimate of the beam propagation length in dielectrics.

From Eqs. (23) and (25), one finds the temperature variation in the beam tail

$$T_e(x) \approx \frac{U_i}{\ln(\sqrt{U_i/m_e} n_a \sigma_{\rm ci}(x_f - x)/v_f)}. \tag{27}$$

As $\sigma_{\rm ci}$ is about 10^{-16}–10^{-17} cm^2, the logarithm is larger than 1 and therefore $T_e < U_i$. It slowly decreases from the front x_f to the source $x = 0$. This formula confirms the hypothesis of weak temperature variation used in Eq. (23). The temperature decrease is a consequence of increasing electron density. The joule heating is decreasing and more energy is spent for the collisional ionization. The electron temperature will increase again as far as the ionization is completed. Numerical simulations presented below demonstrate the square root beam density dependence in agreement with Eq. (25).

The energy dissipation, similar to Eq. (22), contains two terms related to the electron ionization and heating

$$W_{\rm bt} = n_i(0) v_f [\alpha_i U_i + T_e(0)], \tag{28}$$

where $n_i(0)$ and $T_e(0)$ are the electron density and temperature at the beam source. As $n_i(0) \gg n_{i\,\max}$, the electron beam energy dissipation occurs mainly in the beam body and the energy is spent mostly for the ionization. In the case of short electron beams where $n_i(0)$ is less than 10 times $n_{i\,\max}$, the energy dissipation in the front could be dominant.

C. Two-stream instability

The stationary solution described above is strictly speaking unstable. Some of instabilities lead to the beam filamentation, either due to the magnetic field excitation [7] or due to the corrugations of the ionization front [9]. They could be seen only in two- or three-dimensional models. The only instability which might be excited in one spatial dimension is the two-stream instability related to the excitation of the plasma waves in the body of the electron beam. This instability was observed in our numerical simulations and it enhances the energy losses of the beam.

The time of the beam propagation is rather short and only very quickly growing instability can be excited. Then the beam energy spreading and the electron thermal motion in plasma can be neglected and the dispersion equation for the two-stream instability follows from the continuity equations for both electron species, their equations of motion, and from the Poisson equation

$$1 - \frac{\omega_{\rm pb}^2}{\gamma_b^3 (\omega - k_x v_f)^2} - \frac{\omega_{\rm pe}^2}{\omega(\omega + i\nu_e)} = 0, \tag{29}$$

where $\omega_{\rm pb,pe}^2 = e^2 n_{b,e} / \epsilon_0 m_e$ are the plasma frequencies of the beam and the cold electrons. An unstable solution can be found near the plasma resonance with the beam mode: ω

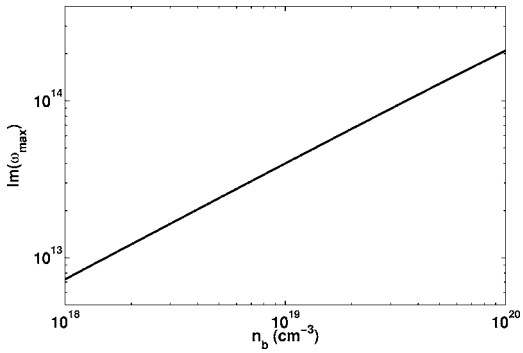

FIG. 2. Dependence of the maximum of the two-stream instability growth rate, Im $\omega_{\max}$ in s^{-1}, on the beam density n_b in cm^{-3} for the electron-atom collision frequency $\nu_e=5$ fs^{-1}.

$\simeq \omega_{pe} \simeq k_{res} v_f$. In the absence of electron collisions the maximum growth rate for the two-stream instability is well known [26]

$$\text{Im}\ \omega_{\max} = \delta_{ts} \equiv 2^{-4/3}\sqrt{3}(\omega_{pb}^2 \omega_{pe})^{1/3}\gamma_f^{-1}. \tag{30}$$

The electron collisions have to be accounted for if $\nu_e > \delta_{ts}$. They decrease the growth rate but do not suppress the instability. The maximum growth rate then becomes Im $\omega_{\max} \approx \delta_{ts}(\delta_{ts}/\nu_e)^{1/2}$. Figure 2 shows the dependence of the maximum instability growth rate on the beam density found from the numerical solution of the dispersion equation for the parameters corresponding to our numerical simulations. The growth rate increases as $n_b^{3/4}$. This dependence agrees with the analytical estimate Im $\omega_{\max} \propto n_b^{1/2} n_e^{1/4}$ if one recalls the fact that $n_e \propto n_b$, according to Eq. (25).

These formulas for the instability growth rate are valid if the beam velocity spread is sufficiently small, Im $\omega_{\max}/\omega_{pe} \gtrsim \Delta v/v_f$. In the opposite case the instability develops in the kinetic regime, the growth rate is much smaller, and it is not interesting for our applications.

The instability might produce a significant energy dissipation if the beam length is large, Im $\omega_{\max} \gtrsim v_f/x_f$, and it has enough time to grow. Then the energy losses associated with the two-stream instability, $\simeq \frac{1}{2}\nu_e \epsilon_0 \langle E_p^2 \rangle$, can be estimated similar to the previous cases. The plasma wave electric field in the instability saturated state follows from the electron beam trapping condition, Im $\omega_{\max} \simeq (eE_p k_{res}/m_e \gamma_f^3)^{1/2}$. In particular, in the collisional regime, $\nu_e > \delta_{ts}$, the saturated electric field reads $E_p \simeq j_b/\epsilon_0 \nu_e$. Then the energy dissipation rate due to the two-stream collisional instability can be estimated as

$$W_{ts} \approx j_b^2/\epsilon_0 \nu_e. \tag{31}$$

For parameters such as in Fig. 2, the condition of the instability excitation is satisfied and it is an important mechanism of the energy dissipation.

IV. RESULTS AND DISCUSSIONS

We present here the results of our simulations of the relativistic electron beam propagation in a plastic target and their interpretations. The beam is 8 μm long and it consists of electrons with velocities uniformly distributed between 0.7 and 0.9 speed of light. The beam comes from an aluminum target considered as a source region and enters the initially neutral plastic (polyethylene) target. The density of the beam is varied between 10^{18} cm^{-3} and 10^{20} cm^{-3}. Our objective here is to study the dependence on the beam density of the ionization front velocity, the dissipation of the beam energy, and the plasma parameters behind the beam.

A. Characteristics of the beam and dependencies on the beam density

1. Ionization process

The ionization process, which takes place in the plastic target during the propagation of the relativistic electron beam, is demonstrated in Fig. 3 at the simulation time 74 fs when the whole beam is already inside the plastic, which begins at 8 μm. The electric field, black curve in panel (a), grows rapidly at the head of the beam. According to Eq. (16), the growth becomes steeper as the beam density increases.

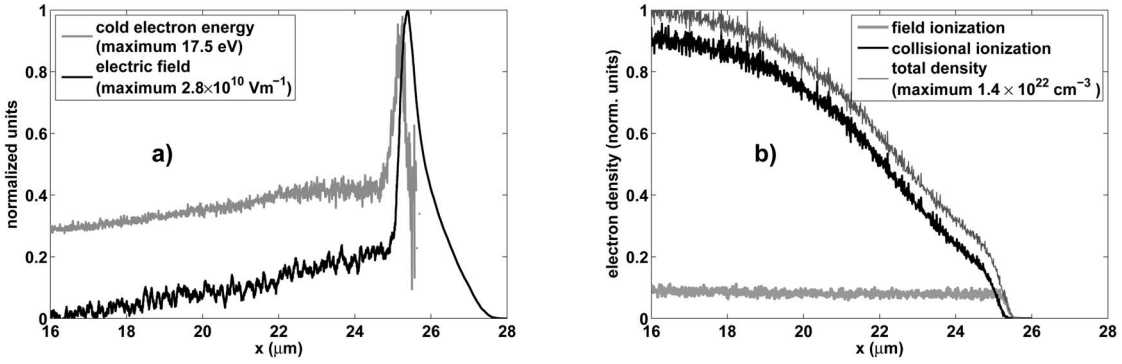

FIG. 3. Demonstration of the ionization processes. The relativistic electron beam with the density 10^{19} cm^{-3} propagates from the left and the snapshot is taken in the time 74 fs. All curves are normalized to the maximum values. In panel (a), the electric field produced by the beam is plotted in black and its maximum is 28 kV/μm, the average kinetic energy of cold electrons is gray, and its maximum is 17.5 eV. In panel (b), the total number of cold electrons is black with the maximum 1.4×10^{22} cm^{-3}. The bold light gray curve demonstrates the density of electrons produced by field ionization, while the thinner dark gray curve demonstrates the density of electrons produced by collisional ionization by the return current electrons. Both these densities are normalized to the total cold electron density.

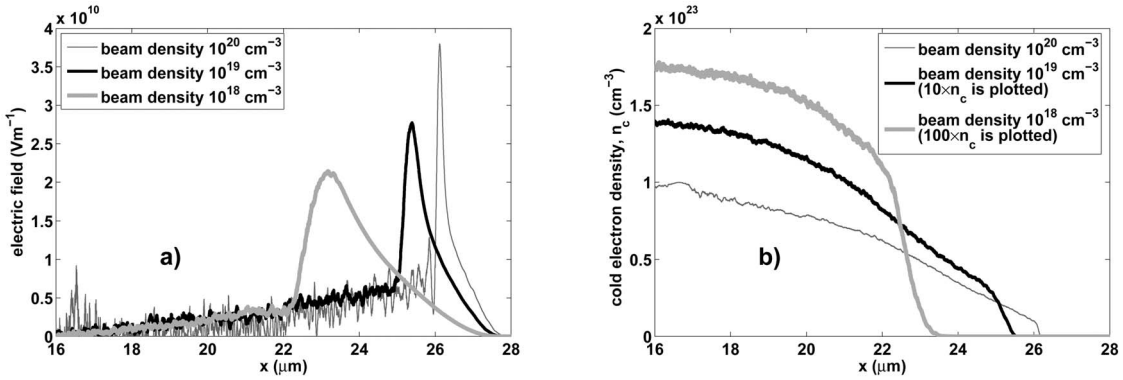

FIG. 4. Comparison of (a) the electric fields and (b) the cold electron densities produced by the field and the avalanche ionization for the relativistic electron beams with densities 10^{18}, 10^{19}, and 10^{20} cm^{-3} at the time 74 fs.

Once the field reaches the value of about 20 kV/μm, the field ionization, bold gray curve in panel (b), starts and the field growth slows down, until it stops. Depending on the beam density, the maximum field in the ionization front is between 23 kV/μm and 38 kV/μm, which agrees well with the analytical results in Fig. 1. This is less than 10% of the atomic field. More than 100 new electrons per one beam electron are produced by the field ionization; see Fig. 1. These new electrons are accelerated by the electric field and neutralize the beam current according to Eq. (13). Then the electric field drops down and the field ionization stops. Collisions of newborn cold electrons play a very important role behind the beam front. It was checked in a special run that if plasma is considered collisionless, the electric field drops down to zero or even changes its sign and starts to oscillate. This is the process of the plasma wake formation behind the electron beam. It operates in a low density plasma but it is suppressed in solid targets because of their high collisionality.

While neutralizing the beam current, cold electrons rapidly gain kinetic energy higher than the ionization potential and start to ionize the neutral atoms behind the front. The collisional ionization frequency for an electron with kinetic energy of tens of eV is very high, of the order of several fs^{-1}. Therefore, the collisional ionization by plasma electrons, thin gray curve in Fig. 3(b), sets up almost immediately after the field ionization. The collisional ionization process is so important that at the end of the ionization front the total cold electron density, black curve in Fig. 3(b), is already doubled, compared with the cold electron density produced just by the field ionization. Moreover, the cold electron density evolution in the beam body confirms the square root behavior found in Eq. (25).

After the initial stage of rapid ionization, the resistivity of plasma drops down and correspondingly the electric field needed for the current neutralization inside the beam is low, about 6 kV/μm. The temperature of cold electrons decreases to 7 eV, below the ionization potential, gray curve in Fig. 3(a), and the collisional ionization rate decreases. Nevertheless, the ionization behind the ionization front persists, the density of cold electrons increases, and the resistivity decreases a few times. Finally, behind the beam, the electric field drops down to zero, as the current density of the beam has been neutralized, and both the heating of plasma and the further increase of number of cold electrons stop there.

The density of the new free electrons produced by the electric field ionization is approximately 10% of the total density of new electrons at the tail of the beam for all three beam densities. The electric field ionization dominates the collisional one in the head of the beam confirming the hypothesis of Sec. III A. It defines the velocity of ionization front. However, the collisional ionization by the return current takes place in the whole region behind the ionization front and consequently produces from 80% to 90% of free electrons.

2. Dependence on the beam density

When comparing the electric field induced by the beam in the plastic target, it is observed in Fig. 4(a) that with the decrease of the beam density, the maximum electric field in the ionization front also decreases, while the thickness of the ionization front increases. This is in agreement with the analytic model described by Eqs. (16) and (21) and shown in Fig. 1. A low amplitude of the electric field implies a low field ionization rate and therefore the thickness of the ionization front must be bigger to provide the field with more space for ionization and production of enough new cold electrons. For all three beam densities, a distinct change in the slope of the cold electron density is observed just behind the ionization front. It corresponds to the switch from electric field to collisional ionization.

The position of the ionization front, in Fig. 4(a), depends on the beam density. This is due to the dependence of the ionization front velocity, v_f, on the beam density, demonstrated in Fig. 1. The front velocity is smaller than the velocity of fastest beam electrons. It can be defined as the mean velocity of the beam electrons inside the strongest field region of the ionization front. The number of fast electrons at the head of the beam creating the strong field, which ionizes the matter, depends weakly on the beam density. Therefore, when the density is lower, the velocity distribution of the beam electrons inside the ionization front contains more slower electrons, and the propagation of the ionization front is correspondingly slower.

For the beam densities 10^{18}, 10^{19}, and 10^{20} cm^{-3}, the densities of cold electrons behind the beam are about 1700

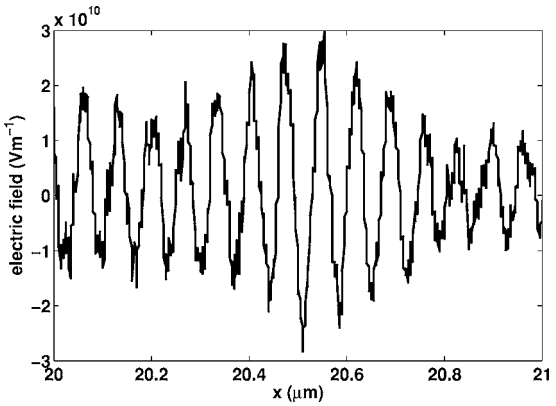

FIG. 5. Details of the oscillating electric field from Fig. 4(a), which is observed during the propagation of the beam with the density 10^{20} cm^{-3}. The wavelength of the oscillations is about 70 nm and they are explained by the two-stream instability.

times, 1400 times, and 1000 times the beam density, respectively; see Fig. 4(b). We must point out that the cold electron density for the beam density 10^{20} cm^{-3} could be even higher if the secondary ionization will be allowed in the model. However, we do not expect any dramatic change in the results. Even if the second outermost shell of carbon will be completely ionized, the cold electron density would increase only by 30%.

3. Two-stream instability

The electric field presented in Fig. 4(a) was smoothed over an interval of about 0.1 μm. For the beam densities 10^{18} and 10^{19} cm^{-3}, the nonaveraged field is similar but more noisy. For the beam density 10^{20} cm^{-3}, the average field is accompanied by regular oscillations demonstrated in Fig. 5. Their wavelength is about 70 nm and their amplitude is comparable with the electric field in the ionization front. This oscillating field is due to the two-stream instability. Its maximum growth rate (30) corresponds to the electron plasma waves with the phase velocity equal to the velocity of the beam $\omega_{pe}/k_{res} \simeq v_f$; see Fig. 2. The frequency of the oscillating field calculated from the simulation data is about 18.5 fs^{-1}, which agrees reasonably well with the electron plasma frequency that is about 18 fs^{-1}.

The maximum growth rate of the two-stream instability increases with the plasma density and in the case of the beam density 10^{20} cm^{-3}, the growth rate can be as high as Im $\omega \sim 1$ fs^{-1}. It is comparable to the collisional frequency of cold electrons which is also of the order of 1 fs^{-1}. For the lower beam densities 10^{19} and 10^{18} cm^{-3}, the two-stream instability was not observed. The growth rates are 3.3 and 10 times smaller, respectively, in these two cases and it has no time to develop during the simulation. Also, the instability growth rate decreases in later times because of beam energy losses.

4. Heating of thermal electrons

The average drift velocity of cold electrons streaming against the beam and their average kinetic energy are presented in Fig. 6. In the region behind the electron beam, where the average velocity is zero, the average energy corresponds to the plasma temperature. The drift velocity attains its maximum in or slightly behind the ionization front and then it gradually decreases to zero. There is only a small difference in the return current drift velocity for the different beam densities. The higher current needed to neutralize the beam with higher density is therefore associated with higher cold electron density.

The average cold electron energy also attains the maximum in the ionization front but we recall that the number of cold electrons is strongly increasing behind this point due to collisional ionization. Then the kinetic energy of electrons decreases below the ionization potential and it remains at this level throughout the beam. The case of the beam density 10^{20} cm^{-3} is an exception. Here additional heating at the end and behind the beam is due to the two-stream instability.

The energy distribution function of cold electrons is shown in more detail in Fig. 7 for the lowest and the highest beam density at the simulation time 74 fs. The case of the beam density 10^{19} cm^{-3} is very similar to the case of the beam density 10^{18} cm^{-3}. The tail of the beam is at the spatial position of about 16 μm and the distribution of cold electrons behind the beam is almost Maxwellian for the beam densities 10^{18} and 10^{19} cm^{-3}. It is established due to the elastic and ionizing collisions. For the beam density 10^{20} cm^{-3},

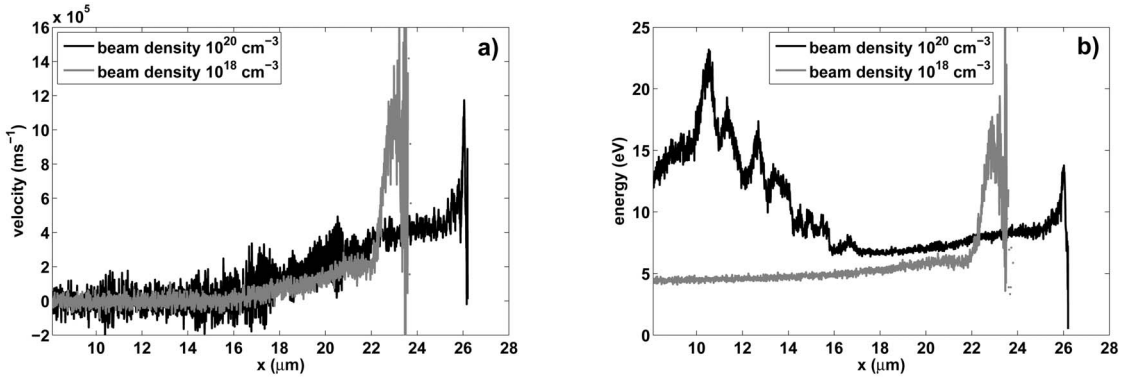

FIG. 6. (a) Average cold electron drift velocity in the direction opposite to the beam propagation and (b) the average cold electron energies at the time 74 fs. The beam is propagating from the left, the plastic part of the target begins at 8 μm, and the end of the beam is at about 16 μm.

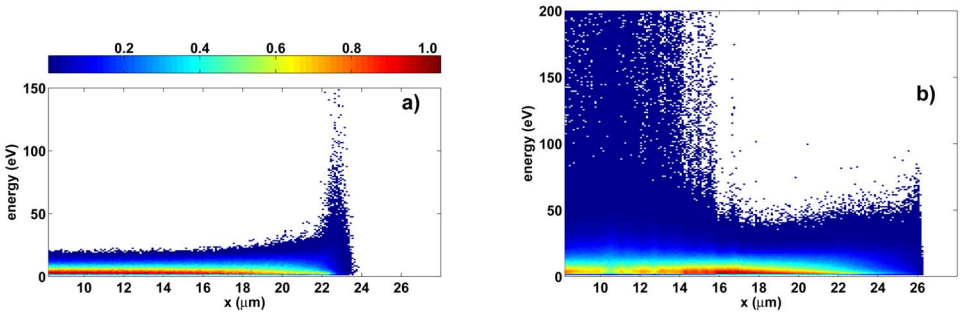

FIG. 7. (Color online) Energy distribution of cold electrons generated by the field and the collisional ionization in a plastic target at the simulation time 74 fs for the beam densities (a) 10^{18} cm^{-3} and (b) 10^{20} cm^{-3}. The plots are normalized to the maximum values.

the distribution function demonstrates a high energy tail related to acceleration of plasma electrons in the electric field generated by the two-stream instability.

B. Temporal evolution of the beam and plasma parameters

The simulation results presented above at the time of 74 fs demonstrate general characteristics of the beam propagation. The temporal evolution of the average beam and plasma parameters is shown in Fig. 8. The simulation results (solid lines with markers) are compared with the results of the analytical model (dashed lines). Although the qualitative behavior is similar, there are some evident quantitative differences which are explained below.

The analytical approach assumes a stationary situation where the beam has already evolved so that only the fastest electrons can penetrate the peak field and the fast electrons that lose their kinetic energy in the ionization front are always replaced by new fresh ones. In the simulation, there are electrons from the whole range of velocities at the head of the beam initially. The fastest ones propagate in front of the field and do not lose almost any energy. The spatial profile of the beam density is smoothed, linearly increasing from zero to the maximum density on the distance of 1 μm, at the beginning of the simulation. Also, in the simulation, the source of fastest electrons in the beam is not infinite and the energy losses play an important role on the longer time scales.

1. Temporal evolution of the average characteristics

The maximum electric field in the ionization front, Fig. 8(a), increases with the beam density and, in the simulation, it remains almost constant during the whole time. It agrees rather well with the predictions of the analytical model. The thickness of the ionization front presented in panel (b) was measured from the absolute head of the beam to the point where the electric field attains its maximum. The initial front thickness for the beam densities 10^{19} and 10^{20} cm^{-3} agrees well in the simulation and in the analytical approach. For the beam density 10^{18} cm^{-3}, the analytical model overestimates the thickness two times because it neglects the collisional ionization which contributes already in the ionization front. The thickness of the ionization front is observed to grow with time. This is due to precursor electrons that propagate at the beam head in front of the electric field. These electrons keep, during the whole simulation, approximately their initial velocity which is close to 0.9 velocity of light. The maximum electric field propagates, on the other hand, with the front velocity and therefore the thickness of the ionization front increases with time.

In the simulation, the front velocity, Fig. 8(c), was calculated from the positions of the maxima of the electric field in two different times. For the two higher beam densities, the field peaks are very narrow and therefore the front velocity is calculated with enough precision using this approach. For the lowest beam density, however, the region around the electric field maximum is significantly wider and therefore the velocity is calculated with less precision and there is an error of approximately 2×10^{6} m/s. Another possible approach is to calculate the average front velocity from the widening of the ionization front. As stated previously, the ionization front widens due to the difference in the velocity of the precursor electrons (0.9 velocity of light) and the peak field (the front

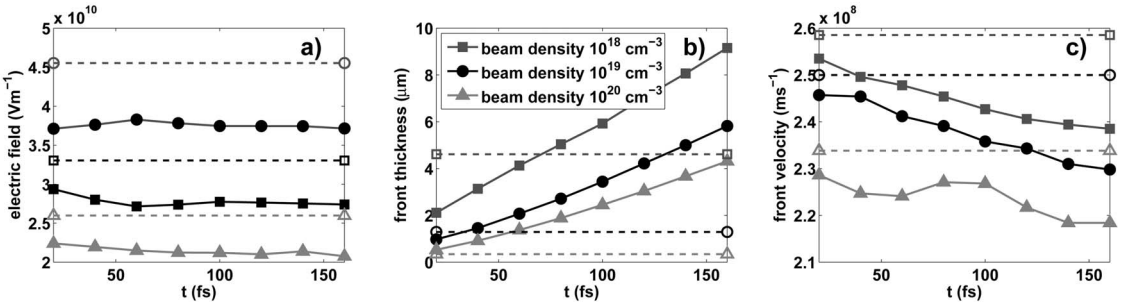

FIG. 8. Temporal evolution of (a) the peak electric field induced by the beams propagating inside the plastic target, (b) the thickness, and (c) the velocity of the ionization front. The ionization front thickness is measured from the position of the beginning of the beam to the position of the field maximum. The front velocity is calculated from the positions of the field maxima in two adjacent times. Solid lines with markers represent numerical results; dashed lines with the corresponding markers represent the values given by the analytical model.

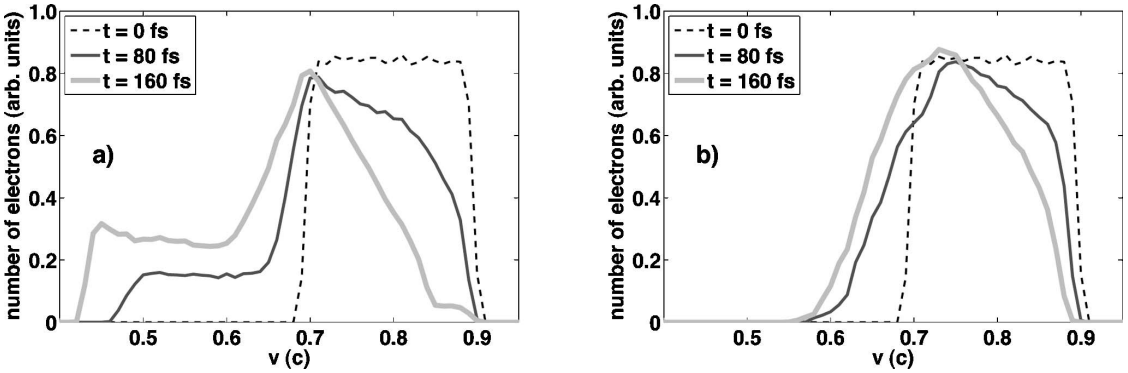

FIG. 9. Temporal evolution of beam velocity distribution function for the beam densities (a) 10^{18} cm^{-3} and (b) 10^{20} cm^{-3}. The distribution is initially uniform and all electrons are equally decelerated. Further in time, only faster electrons are at the head of the beam where the electric field is higher and they are decelerated more strongly.

velocity). With this approach, the average front velocity at the time between 20 fs and 160 fs is 2.2×10^8 m/s, 2.36×10^8 m/s, and 2.43×10^8 m/s for the beam densities 10^{18} cm^{-3}, 10^{19} cm^{-3}, and 10^{20} cm^{-3}, respectively.

The initial values of the front velocity in the simulations are in reasonable agreement with the ones calculated analytically. With time, however, the front velocity in the simulation decreases and the beam propagation is slower. The decrease in the front velocity is associated with the decreasing number of the fastest electrons in the beam and hence also with the dissipation of the beam energy. The temporal evolution of the beam velocity distribution function is demonstrated in Fig. 9.

2. Beam velocity distribution

The evolution of the beam velocity distribution with time is the strongest for the beam density 10^{18} cm^{-3}; see Fig. 9(a). As in the beginning of the simulation, electrons from the whole range of velocities, i.e., from 0.7 to 0.9 velocity of light, are at the head of the beam in the ionization front; these electrons are losing energy almost equally. Later in time, however, preferentially the fastest electrons are slowed down, as they are mostly the ones which propagate faster than the ionization front and therefore they can get into the regions where the field is the highest. At the simulation time 160 fs, the precursor electrons are also clearly seen here. They are not stopped in the ionization front and propagate freely in front of it.

The evolution of the beam velocity distribution for the higher beam density 10^{20} cm^{-3}, panel (b), exhibits similar features, however, the changes in the distribution are much weaker. There are two reasons for this slower evolution. First, when integrating the electric field in the ionization front for different beam densities, it was found that the lower the beam density, the higher the electric potential. The second reason is that the higher the front velocity, the shorter the time needed for an electron to cross the front. Both these factors together result in the energy losses that are more significant at lower beam densities. Therefore, when comparing the distributions in Fig. 9 for the different beam densities, not only the numbers of decelerated electrons but also the velocities of the slowest electrons are different.

3. Beam current evolution and the current neutralization

The evolution of the beam current density is demonstrated in Fig. 10. At simulation time 80 fs, the return current is also shown. The current neutralization is quite good except the smallest density and the front region. The temporal evolution

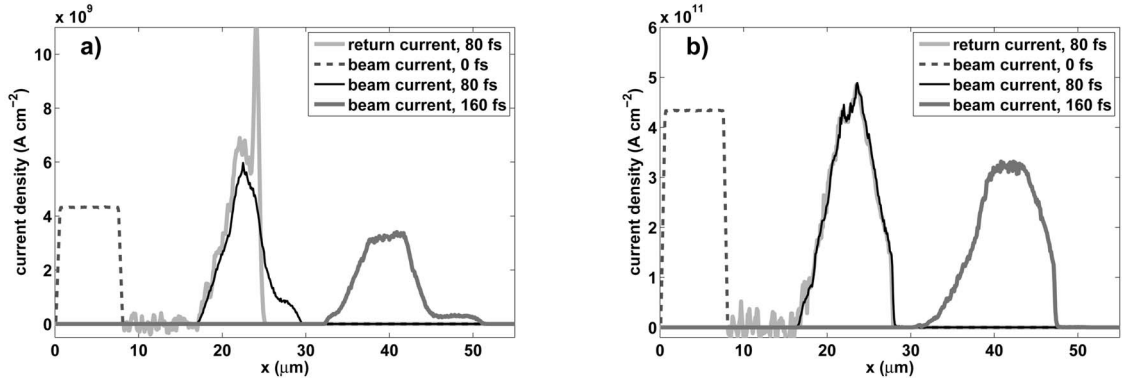

FIG. 10. Temporal evolution of the beam current density for the beam densities (a) 10^{18} cm^{-3} and (b) 10^{20} cm^{-3}. The return current is also shown at the time 80 fs to demonstrate the current neutralization. The beam electrons that are slowed down in the peak field in the ionization front appear inside the beam and increase its current density. Precursor electrons are seen for the beam density 10^{18} cm^{-3}.

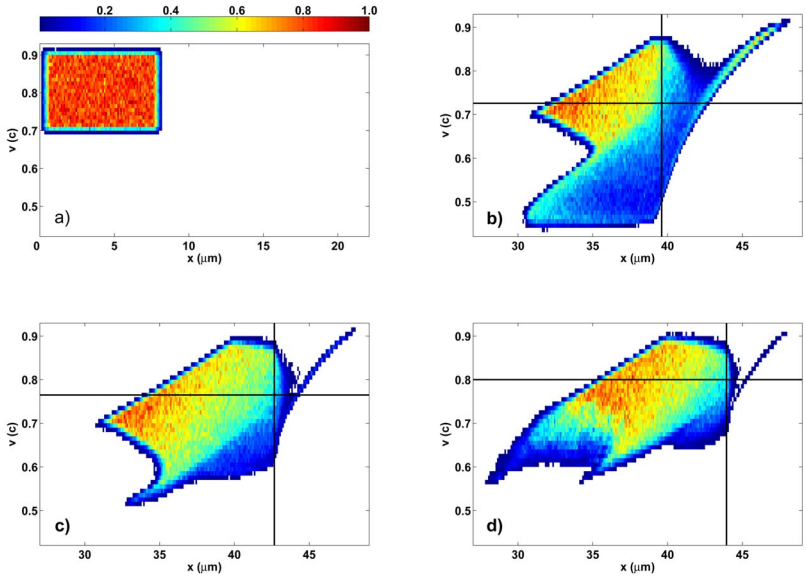

FIG. 11. (Color online) Distribution of the beam electrons in the phase space at (a) the initial moment and at the time 148 fs for the beam densities (b) 10^{18} cm^{-3}, (c) 10^{19} cm^{-3}, and (d) 10^{20} cm^{-3}. Colors represent the normalized number of beam electrons and the figures in each panel cover equal areas. The velocity is normalized to the velocity of light. The horizontal lines represent the ionization front velocity; the vertical lines represent the position of the ionization front.

of the beam current density is due to two effects: The ballistic evolution and the electric fields. At the head of the beam in the ionization front, the fast electrons are decelerated below the average velocity of the beam and they are caught up by the rest of the beam, increasing the beam density behind the ionization front. As the deceleration of the beam electrons is the strongest for the lowest beam density 10^{18} cm^{-3}, the beam current density behind the ionization front is increased in this case by almost 40%. In later time, however, the ballistic spreading predominates and the current density decreases inside the whole beam.

In Fig. 10(a), the precursor electrons in the time 160 fs are clearly distinguishable. The electric field induced by these electrons is independent of the beam density and its value in this time is about 9 kV/μm. The average separation of the precursor electrons from the region, where the quasineutrality is restored, is approximately half the difference between the initial thickness of the ionization front and the thickness in the time 160 fs, i.e. 3.6 μm for the beam density 10^{18} cm^{-3}. Substituting this thickness and the electric field stated above into the Poisson equation (7) one can estimate the average density of the precursor electrons. For the beam density 10^{18} cm^{-3}, it is about 14% of the initial beam density, while for the beam densities 10^{19} cm^{-3} and 10^{20} cm^{-3}, it is only 2.1% and 0.2%, respectively. Therefore, the current of precursor electrons is limited by the value of $\sim$1 GA/cm^2.

4. Energy dissipation

The distribution of the beam electrons in the phase space is demonstrated in Fig. 11 at the simulation time 160 fs for all three beam densities. The figure in each panel covers the same area and the color represents the same number of simulation electrons in all four panels. The horizontal line in panels (b), (c), and (d) represents the actual front velocity, while the vertical line denotes the position of the peak electric field in the ionization front. In panel (a), the initial beam distribution is plotted for comparison. In this panel, the whole beam is in aluminum layer and its distribution is uniform with only slightly smoothed borders. At the time 160 fs, the rhomboid-like shape of the distribution is due to the ballistic evolution. Fast electrons with the velocity higher than the front velocity penetrate into the ionization front and are slowed down by the electric field. They leave the front and are caught up by the beam again. They are accumulated behind the ionization front and form a peak which is seen in the current density plots in Fig. 10. In all three panels, the precursor electrons are clearly seen.

The lowest beam density, 10^{18} cm^{-3}, corresponds to the highest energy dissipation. At the time 160 fs, there are no more electrons with the velocity 0.9 velocity of light in this distribution and therefore the velocity of the ionization front is already relatively low. On the other hand, as the front velocity is the lowest in this case during the whole simulation, the fastest electrons get into the ionization front from the beam earlier, they propagate with the front for a longer time, and their energy losses are the highest. For the highest beam density, 10^{20} cm^{-3}, the tail of the beam distribution is also significantly disturbed. This is the result of the two-stream instability.

In Fig. 12, the energy losses of the beams are demonstrated against the propagation distance measured at the position of the ionization front. The beam with the density 10^{18} cm^{-3} loses about 50% of its total energy on the distance of 40 μm. This explains why the front velocity of this beam decreases significantly. The energy lost by the beam is transferred into the kinetic energy of cold electrons and as long as there are enough neutral atoms in the target, this energy is used for additional ionization.

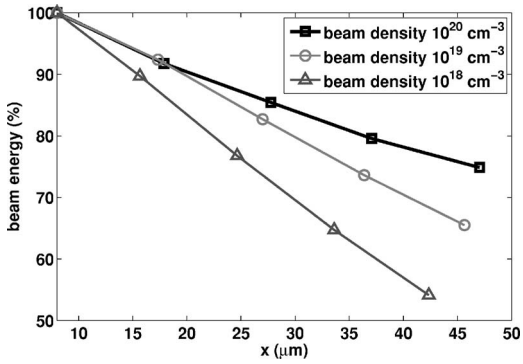

FIG. 12. Electron beam energy losses (in percents of the initial energy) versus the propagation distance. Initial energy of the beam decreases almost linearly in all three cases and the energy dissipation is stronger the lower the beam density. The beam with the density 10^{18} cm^{-3} loses 50% of energy on the distance of 40 μm.

As the electric field behind the ionization front is approximately the same for all three beam densities, Fig. 4 (except for the highest beam density where the two-stream instability is excited), the field inside the ionization front is responsible for different energy losses. From the energy losses of the beam in Fig. 12, we can calculate the average stopping power acting on a beam electron. It is about 4.9, 3.6, and 2.4 keV/μm for the beam densities going up from 10^{18} to 10^{20} cm^{-3}. This is more than ten times larger than the classical stopping power of a single electron due to the binary collisions, which is less than 0.3 keV/μm. It is a clear manifestation of the collective effects.

C. Scaling of the beam propagation characteristics

The velocity distribution of the beam electrons chosen here allows one to see clearly the various physical processes. However, it is not as relativistic as the ones obtained nowadays in high intensity laser target interaction experiments. The energy flux corresponding to the highest density beam here is only about 10^{17} W/cm^2. However, the calculations with more energetic uniform beam distributions (with velocities between 0.9 and 0.99 velocity of light) confirm that the physical processes are similar to the ones described above. Only the velocity of the ionization front is higher and the energy losses of the beam do not significantly influence its propagation on the temporal scales which we are able to simulate.

Finally, we want to point out that our simulations are currently limited to the range of the beam current densities 4–400 GA/cm^2 used here. The lower or higher beam densities can be only accessed by the analytical model at the moment. In particular, for higher densities one or two more electrons per atom will be liberated due the collisional ionization. Because of increase in the ionization potential, the cold electron temperature will increase, which will lower the collisionality. Moreover, as the additional ionization will be more difficult, the electric field behind the ionization front may be higher and this will increase the energy losses of the beam as well. Finally, the two-stream instability (as well as other multidimensional instabilities) will be excited more strongly increasing even more the stopping power. For the lower electron current beam densities, the electric field ionization will not provide a sufficient number of cold electrons for the return current and the stopping of the beam by the electric field will be very strong.

V. CONCLUSIONS

We have presented a theoretical model and numerical simulations describing the transport of a high current relativistic electron beam in dielectric targets. Our analytical model for the ionization front is based on the approach described in Refs. [9,11], but the initial velocity distribution function for the beam electrons is different. Our model takes into account the processes of the field ionization in the head of the electron beam and the subsequent collisional ionization of the insulator by secondary electrons. The processes of current and charge neutralization take place in the ionization front and its thickness is adjusted self-consistently. The heating of the plasma electrons by the return current is identified as a major source of the secondary ionization and the beam energy losses. The theoretical model has been compared with a simulation code based on the PIC algorithm. It includes the ionization processes induced by the self-consistent electric field and the secondary plasma electrons. It also includes the elastic electron-atom and Coulomb collisions with realistic cross sections. Simulations show that the self-consistent electric field in the beam head plays an important role in the fast electron transport, defining the average beam velocity and providing the initial population of plasma electrons. Its amplitude is saturated at the level of about 10% of the atomic electric field and it never provides a complete ionization. The density of plasma electrons created in the ionization front is typically 100 times the electron beam density. The collisional ionization takes place mainly in the beam body where the electric field is strongly reduced.

The numerical simulations and the analytical model show that the average electron beam velocity is an increasing function of the beam current density for the currents larger than a few tens of GA/cm^2. Such a dependence $v_f(j_b)$ may cause a filamentation instability at the ionization front predicted in [9] and already observed in the experiment [10]. This two-dimensional effect is not described within our one-dimensional model, which nevertheless demonstrated an important effect of excitation of a large-amplitude plasma wave due to the two stream beam-plasma instability. It is excited at the current densities $\sim$400 GA/cm^2 and it enhances the beam dissipation rate and leads to acceleration of plasma electrons to keV energies.

The simulations demonstrate a complicated beam electron dynamics related to the ionization process in the beam head. The fastest electrons, which are moving with the velocities higher than the ionization front, are entering the front and losing a significant part of their energy to support the strong electrostatic field and the ionization process. Therefore, the efficient beam propagation is maintained as long as the electron beam can supply enough of these energetic electrons. For an electron beam of a finite length the propagation would be strongly inhibited at the moment when all energetic elec-

trons will cross the front. This effect can be used to control the propagation length and the deposition rate of high current electron beams.

Finally, a significant electron heating takes place in the beam tail behind the ionization front. The level of electron plasma temperature is controlled by the collisional ionization and it is kept below the ionization potential as long as the ionization is not completed. This process could play an important role also in metallic target providing an increased ionization level for higher beam currents. Because of computational limitations, our numerical simulations were restricted here to relatively low energy fluxes below 10^{18} W/cm^2, where the energy losses are relatively high. This allowed us to compare the numerical results with the analytical predictions for the realistic current densities at a relatively short propagation distance. However, the analytical model is valid for much higher energy fluxes and it predicts a decrease of the beam energy losses at higher intensities.

ACKNOWLEDGMENTS

This work was supported by the COST Office in the frame of the project STSM-P14-01494.

APPENDIX: ELASTIC ELECTRON-ATOM AND COULOMB COLLISIONS

Random sampling of the deflection angle χ for the elastic electron-atom collisions from the differential cross section (3) was performed with a random number R uniformly distributed between 0 and 1 using the formula

$$\cos\chi = \varepsilon^{-1}[\varepsilon + 2 - 2(1+\varepsilon)^R]. \tag{A1}$$

Similarly, for the Coulomb collisions, the deflection angle was sampled from the distribution (4) as follows:

$$\cos\chi = 1 + A^{-1}\ln R. \tag{A2}$$

The azimuthal angle of the collision plane ψ is uniformly distributed between 0 and 2π for both types of collisions.

Supposing that the velocities of particles before the collision are $\boldsymbol{v_1}$ and $\boldsymbol{v_2}$, the post-collision velocities for the electron-electron collision were calculated according to the formulas [20]

$$\boldsymbol{v}'_{1,2} = \boldsymbol{v}_{1,2} \mp [\boldsymbol{g}(1-\cos\chi) + \boldsymbol{h}\sin\chi]/2, \tag{A3}$$

where $\boldsymbol{g}=\boldsymbol{v_1}-\boldsymbol{v_2}$ is the relative velocity. The vector $\boldsymbol{h}$ is designed to maintain the energy conservation. Its Cartesian components are

$$h_x = g_\perp \cos\psi,$$

$$h_y = -(g_x g_y \cos\psi + g g_z \sin\psi)/g_\perp,$$

$$h_z = -(g_x g_z \cos\psi - g g_y \sin\psi)/g_\perp, \tag{A4}$$

where $g_\perp = (g_y^2 + g_z^2)^{1/2}$. For electron-atom and electron-ion collisions, the velocity of atoms and ions was set to zero and their mass to infinity. Correspondingly, the postcollision electron velocity was calculated from Eq. (A3) by setting $\boldsymbol{v_2}=\boldsymbol{0}$ and $\boldsymbol{g}=\boldsymbol{v_1}$.

[1] J. R. Davies, A. R. Bell, M. G. Haines, and S. M. Guerin, Phys. Rev. E **56**, 7193 (1997).
[2] E. E. Fill, Phys. Plasmas **8**, 1441 (2001).
[3] J. J. Santos *et al.*, Phys. Rev. Lett. **89**, 025001 (2002).
[4] S. D. Baton *et al.*, Plasma Phys. Controlled Fusion **47**, B777 (2005).
[5] M. Tatarakis *et al.*, Phys. Rev. Lett. **90**, 175001 (2003).
[6] M. Tabak *et al.*, Phys. Plasmas **1**, 1626 (1994).
[7] E. S. Weibel, Phys. Rev. Lett. **2**, 83 (1959).
[8] F. Califano, F. Pegoraro, S. V. Bulanov, and A. Mangeney, Phys. Rev. E **57**, 7048 (1998).
[9] S. I. Krasheninnikov, A. V. Kim, B. K. Frolov, and R. Stephens, Phys. Plasmas **12**, 073105 (2005).
[10] M. Manclossi, J. J. Santos, D. Batani, J. Faure, A. Debayle, V. T. Tikhonchuk, and V. Malka, Phys. Rev. Lett. **96**, 125002 (2006).
[11] V. T. Tikhonchuk, Phys. Plasmas **9**, 1416 (2002).
[12] L. Gremillet, G. Bonnaud, and F. Amiranoff, Phys. Plasmas **9**, 941 (2002).
[13] J. R. Davies, Phys. Rev. E **65**, 026407 (2002).
[14] J. J. Honrubia, M. Kaluza, J. Schreiber, G. D. Tsakiris, and J. Meyer-ter-Vehn, Phys. Plasmas **12**, 052708 (2005).
[15] R. Lichters, R. E. W. Pfund, and J. Meyer-ter-Vehn, Report No. MPQ 225, Garching, 1997 (unpublished).
[16] A. J. Kemp, R. E. W. Pfund, and J. Meyer-ter-Vehn, Phys. Plasmas **11**, 5648 (2004).
[17] M. Ammosov, N. B. Delone, and V. P. Krainov, Sov. Phys. JETP **64**, 1191 (1986).
[18] D. Bauer, Phys. Rev. A **55**, 2180 (1997).
[19] Y.-K. Kim and M. E. Rudd, Phys. Rev. A **50**, 3954 (1994).
[20] K. Nanbu and S. Yonemura, J. Comput. Phys. **145**, 639 (1998).
[21] R. Mayol and F. Salvat, At. Data Nucl. Data Tables **65**, 55 (1997).
[22] M. Surendra, D. B. Graves, and G. M. Jellum, Phys. Rev. A **41**, 1112 (1990).
[23] A. V. Bobylev and K. Nanbu, Phys. Rev. E **61**, 4576 (2000).
[24] Y. B. Zel'dovich and Y. P. Raizer, *Physics of Shock Waves and High-Temperature Hydrodynamic Phenomena* (Dover, Mineola, NY, 2002).
[25] J. R. Peñano, P. Sprangle, B. Hafizi, W. Manheimer, and A. Zigler, Phys. Rev. E **72**, 036412 (2005).
[26] S. Kainer, J. Dawson, and R. Shanny, Phys. Fluids **15**, 493 (1972).